PCCP

Hybrid DFT investigation of the energetics of Mg ion diffusion in α-MoO₃

Journal:	*Physical Chemistry Chemical Physics*
Manuscript ID	CP-ART-08-2018-005511
Article Type:	Paper
Date Submitted by the Author:	30-Aug-2018
Complete List of Authors:	Barnes, Taylor; Virginia Polytechnic Institute and State University, Wan, Liwen; Lawrence Berkeley National Laboratory, The Molecular Foundry Kent, Paul; Oak Ridge National Laboratory, Prendergast, David; Lawrence Berkeley National Laboratory, Molecular Foundry

Journal Name

Hybrid DFT investigation of the energetics of Mg ion diffusion in α-MoO$_3$†

Taylor A. Barnes,[*a] Liwen F. Wan,[b,c] Paul R. C. Kent,[d] and David Prendergast[b]

Rechargeable batteries that utilize divalent Mg ions as the charge carrier species can in principle achieve substantially greater volumetric energy densities than conventional Li-ion batteries. One significant impediment to the development of commercially viable Mg-ion batteries is the slow rate of Mg ion diffusion through otherwise promising cathode materials. Accurate prediction of the activation energies associated with this diffusion process using density functional theory (DFT) is especially challenging due to self-interaction errors intrinsic to DFT that lead to over-delocalization of the d-electrons. One effective but highly computationally demanding approach to reducing self-interaction errors is the use of hybrid functionals, which incorporate a fraction of exact Hartree-Fock exchange. In this work, we assess the effects of exact exchange on computed activation energies for ion diffusion in one potential cathode material, α-MoO$_3$. In contrast to previous studies that primarily utilize non-hybrid functionals, we perform nudged elastic band calculations in which the nuclear coordinates are fully converged using both hybrid functionals and k-point sampling. It is found that while non-hybrid functionals indicate the existence of thermodynamically accessible channels for bulk Mg ion diffusion in all three dimensions, hybrid functionals predict that some of these channels are largely inaccessible under typical charge/discharge conditions. Furthermore, it is demonstrated that certain commonly used approximations for incorporating the effects of Hartree-Fock exchange are inadequate for this system, including DFT+U calculations and the use of single-point hybrid calculations using atomic positions obtained using non-hybrid functionals.

1 Introduction

The enduring search for improved rechargeable battery technology has motivated interest in the development of batteries that shuttle multivalent ions, rather than the monovalent Li$^+$ ions observed in commercially ubiquitous Li-ion batteries. Of particular promise are magnesium-based batteries[1,2], which can in principle achieve volumetric energy densities substantially greater than those of Li-ion batteries, while utilizing terrestrially abundant magnesium instead of rarer and more expensive lithium[3]. Furthermore, unlike lithium metal, magnesium metal batteries do not exhibit significant dendritic growth at the anode and thus mitigate one of the primary safety concerns associated with lithium-based batteries[4].

A key challenge to the development of commercially viable Mg batteries arises from the strong electrostatic interactions between the ion and its surroundings, which tend to limit the rate of ion shuttling throughout the charge/discharge cycle[2,5]. The development of Mg-based energy storage technologies thus requires identifying electrode materials that provide both sufficient energy density and sufficient facile ionic diffusion in the bulk and across interfaces at acceptable operating temperatures. Identification of a cathode that meets these criteria has proven to be especially difficult, with numerous transition metal oxides and sulfides[1,6–12] being among the materials that have been tested for this purpose.

One cathode material that is considered to be of particular interest is α-MoO$_3$[13–20], which has been investigated for possible use in Mg-ion batteries that utilize nonaqueous[13,15], ionic liq-

[a] Molecular Sciences Software Institute, Blacksburg, Virginia 24060, United States. Tel: +1 540 231 6992; E-mail: tbarnes1@vt.edu

[b] Joint Center for Energy Storage Research, The Molecular Foundry, Lawrence Berkeley National Laboratory, Berkeley, California 94720, United States.

[c] Materials Science Division, Lawrence Livermore National Laboratory, Livermore, California 94550, United States.

[d] Center for Nanophase Materials Sciences, Oak Ridge National Laboratory, Oak Ridge, Tennessee 37831, United States.

uid[15], or gel polymer electrolytes[19]. Using wet nonaqueous electrolytes, α-MoO$_3$ has yielded a cell voltage of approximately 1.7 V and a reversible capacity of 210 mAh/g during slow galvanostatic titration (0.3 A cm^{-2}) over 10 cycles[13]. Despite these promising results, α-MoO$_3$ exhibits a charge/discharge hysteresis that is approximately 3-6 times larger than that observed in V$_2$O$_5$ thin film electrodes[13]. This observation has been interpreted as indicative of extremely slow intercalation kinetics resulting from strong electrostatic interactions between the Mg ions and the metal oxide structure[13], although the detailed thermodynamics of Mg ion diffusion in α-MoO$_3$ remains a subject of investigation[21].

Computational efforts using density functional theory (DFT) have identified several of the diffusive channels that control the rate of diffusion through the bulk material[21]. Because of the well-known challenges associated with the application of semi-local DFT functionals to compute the electronic structure of transition metal materials, these previous efforts incorporated a Hubbard U for the calculation of single-point energies. Using a PBE+U approach, it was found that all activation barriers associated with Mg diffusion through these channels are within the range of 0.6-1.1 eV, suggesting that Mg diffusion should be observed in all three dimensions through the bulk material[21].

The commonly used local and semi-local DFT functionals struggle to accurately treat electrons from the 3d series and beyond[22–27] due to self-interaction error and over-delocalization of the d electrons. It is thus an important question whether local or semi-local DFT approaches can reliably represent the localized Mo 4d electrons in α-MoO$_3$ and the potentially varied oxidation state of these atoms during ionic diffusion. Although the application of a Hubbard U term can mitigate some of the failures of semi-local DFT, the optimal choice of Hubbard U for each species is unclear, and numerous values have been used in the literature[22,24]. A more reliable method for correcting self-interaction errors is the use of hybrid functionals; regardless of this, the application of hybrid functionals is highly computationally demanding, resulting in many studies that utilize non-hybrid functionals[9,10,21,28–42], and far fewer that incorporate the use of hybrid functionals[43–47].

In this paper we investigate the pathway and energy barriers for Mg ion diffusion in bulk α-MoO$_3$ using hybrid DFT functionals. It is expected that hybrid functionals should yield a more accurate treatment of the localized Mo d electrons, providing both an improved understanding of Mg ion diffusion in α-MoO$_3$ and an opportunity to compare the results of semi-local and hybrid functionals for this system. Although previous studies of condensed-phase systems have incorporated the use of hybrid functionals for single-point calculations[48–54] and geometry optimizations[55–58], utilization of hybrid functionals in complex calculations remains computationally demanding. Despite this challenge, we present the results of nudged elastic band (NEB) calculations in which the nuclear coordinates are fully relaxed using hybrid functionals. This is accomplished through the use of recent improvements to the implementation[59] and methodology[60] of hybrid DFT calculations in the Quantum ESPRESSO code.[61]

2 Methods

The primary computational method used in this paper is DFT. Although DFT is formally exact, practical calculations require the use of approximate formulations of the exchange-correlation functional. Local and semi-local functionals are among the most commonly used functional forms for solid-state calculations, but suffer from the limitations previously described. These limitations can be partially corrected by replacing the approximate exchange-correlation functional with a hybrid exchange-correlation functional,

$$v_{\text{xc}}^{\text{hybrid}}\left[\{\psi_j\};\mathbf{r}\right] = v_{\text{c}}\left[\rho;\mathbf{r}\right] + v_{\text{x}}^{\text{LR}}\left[\rho;\mathbf{r}\right] + (1-\alpha)v_{\text{x}}^{\text{SR}}\left[\rho;\mathbf{r}\right] + \alpha\hat{K}\left[\{\psi_j\};\mathbf{r}\right].$$

(1)

where $v_{\text{c}}\left[\rho;\mathbf{r}\right]$ is the correlation functional, $v_{\text{x}}^{\text{LR}}\left[\rho;\mathbf{r}\right]$ is the long-range component of the exchange functional, $v_{\text{x}}^{\text{SR}}\left[\rho;\mathbf{r}\right]$ is the short-range component of the exchange functional, $\hat{K}\left[\{\psi_j\};\mathbf{r}\right]$ is the exact (Hartree-Fock) exchange, and α is the fraction of exact exchange used. Among other advantages, hybrid functionals tend to significantly reduce the magnitude of self-interaction error.

Evaluation of the exact exchange requires the calculation of a large number of integrals,

$$(\hat{K}\left[\{\psi_j\};\mathbf{r}\right]\psi_i)(\mathbf{r}) = -\sum_{j=1}^{n_{occ}}\left[\psi_j(\mathbf{r})\int\frac{\psi_j^*(\mathbf{r}')\psi_i(\mathbf{r}')}{|\mathbf{r}'-\mathbf{r}|}d\mathbf{r}'\right],$$

(2)

which is the most computationally demanding component of a typical hybrid DFT calculation. This high expense has resulted in only limited application of hybrid functionals to complex many-atom problems, although a number of methods have been developed with the intention of mitigating the computational cost associated with the use of hybrid functionals[62–65]. In this paper we make use of two technical improvements to their utilization: an improved parallel implementation of Eqn. 2 in the Quantum ESPRESSO code[59] and the adaptively compressed exchange operator algorithm[60] which requires fewer evaluations of the exact exchange integrals during the DFT calculation. These two improvements enable an approximately order of magnitude improvement in time to solution for the calculations presented in this paper.

Numerous less computationally demanding approaches have been developed for improving upon local and semi-local DFT[66–69], with the DFT+U method being especially popular[70]. This approach introduces an additional term in the energy expression,

$$E^{\text{DFT+U}} = E^{\text{DFT}} + \frac{U-J}{2}\sum_{\sigma}Tr\left[\rho^\sigma - \rho^\sigma\rho^\sigma\right]$$

(3)

where σ labels the spin, ρ^σ is the spin-dependent on-site density matrix, and U and J are parameters introduced by the Hubbard model. This term can improve the treatment of the d electrons, but at the expense of introducing the unknown parameter $U_{\text{eff}} = U - J$. These parameters are in principle site-dependent, but are commonly assigned on a per-species basis only.

In the remainder of this paper, we compare and analyze activation barriers for Mg-ion diffusion obtained using semi-local DFT, hybrid DFT, and the DFT+U method. All calculations throughout

the paper are performed using a $3 \times 1 \times 3$ α-MoO$_3$ supercell, a $2 \times 2 \times 2$ k-point grid, an energy cutoff of 80 Ry for the generation of the plane wave basis set, a cutoff of 90 Ry for the evaluation of the exact exchange operator, and with gaussian smearing of 0.0025 Ry for the Brillouin-zone integration. All calculations use a fixed cell dimension of 11.793 Å $\times$ 13.935 Å $\times$ 11.126 Å, which was obtained from previous calculations using the van der Waals (vdW) corrected optB86b-vdW functional [21]. Note that as emphasized in Ref. 21, a vdW corrected functional is necessary for accurate prediction of the interlayer spacing in α-MoO$_3$. For a fixed cell dimension, the use of a vdW correction is not observed to significantly affect the accuracy of computed activation barriers of Mg ion diffusion; the differences in activation energies obtained using PBE and optB86b-vdW functionals are found to be within 50 meV. All calculations are performed using the NERSC Cori Phase II system [71].

3 Results

3.1 Analysis of an α-MoO$_3$ supercell

Fig. 1(a) compares the electron density of an α-MoO$_3$ supercell obtained using the semi-local PBE functional [72] versus the hybrid HSE functional [73]. In order to allow for straightforward comparison of the densities, both the PBE and HSE results are obtained using a PBE-optimized nuclear geometry; throughout this paper, we use the notation HSE//PBE to indicate a single-point HSE calculation that is performed using a PBE-relaxed geometry. The results in Fig. 1 are obtained using Schlipf-Gygi norm-conserving pseudopotentials [74,75]. Relative to PBE, the HSE//PBE results can be seen to increase the electron density in the vicinity of the oxygen nuclei, while decreasing the electron density in the vicinity of the molybdenum nuclei. This shift in electron density corresponds to an increase in the ionic character of the Mo-O bonds, which is consistent with the tendency of hybrid functionals to yield bonds that are more ionic than those obtained using GGA functionals [76–78].

Fig. 1(b) provides a more quantitative description of the shift in electron density caused by the introduction of exact exchange. The figure provides the total integrated charge difference within a sphere centered on various atoms and for spheres of varying radius R. The pristine α-MoO$_3$ system includes three symmetrically distinct oxygen atoms, which we denote as O$_{(1)}$, O$_{(2)}$ and O$_{(3)}$, corresponding to Wyckoff positions of (0.0362, 0.2257, 0.25), (0.5228, 0.0880, 0.25), and (0.5003, 0.4340, 0.25), respectively. Each type of oxygen atom, in addition to the molybdenum atoms and the magnesium ion, exhibits an extremum at approximately $R = 1.0$-1.2 Å, the magnitude of which we interpret as a rough estimate of the difference between the PBE and HSE atomic charges. Using this estimate, the HSE//PBE charges of the O$_{(1)}$, O$_{(2)}$, and O$_{(3)}$ nuclei are 0.029, 0.040, and 0.052 electrons higher than the PBE charges, respectively. Conversely, the charge on the molybdenum is approximately 0.104 electrons lower when using exact exchange. For systems that include a Mg within the α-MoO$_3$ supercell, a relatively small difference of 0.012 electrons is observed between the HSE//PBE and PBE charges on the Mg, consistent with the ionic nature of this atom and the lack of an energeti-

Table 1 Activation barriers (forward / reverse), calculated using the PBE, PBE0, and HSE functionals and reported in eV

	PBE	PBE0	HSE
Path 1	0.85 / 0.71	0.74 / 0.64	0.73 / 0.64
Path 2	0.92 / 0.79	1.57 / 1.48	1.53 / 1.44
Path 3	0.80 / 0.80	1.38 / 1.38	1.39 / 1.39

cally accessible atomic Mg 3s state for hybridization with nearby oxygen anions.

3.2 Analysis of Mg-ion diffusion paths

Fig. 2(a) illustrates three paths for Mg-ion diffusion that have been previously identified [21]. Paths 1 and 2 correspond to Mg diffusion within the interlayer gap between the MoO$_3$ bilayers, while Path 3 corresponds to intralayer diffusion. In order to better understand the energetics of Mg ion diffusion in α-MoO$_3$, NEB calculations are performed on each pathway using the semi-local PBE functional and the hybrid PBE0 [79,80] and HSE functionals. For each of these NEB calculations, the nuclear coordinates are fully relaxed using the corresponding functional. The results of the NEB calculations are provided in Fig. 2(b), and the corresponding activation barriers are listed in Table 1. When the semi-local PBE functional is used, all activation barriers are found to be in the range of approximately 0.7-0.9 eV, with the largest barrier corresponding to the forward reaction of Path 2. These results are consistent with previous calculations performed using the non-hybrid optB86b-vdW functional [21]. The use of the hybrid functionals yields results that are substantially different from those of the PBE functional. Relative to the PBE results, the HSE functional produces an activation barrier for Path 1 that is approximately 0.1 eV lower, and activation barriers for Paths 2 and 3 that are approximately 0.6 eV higher. Consequently, the HSE activation barrier for Paths 2 and 3 is roughly double that of Path 1. The PBE0 and HSE functionals produce very similar activation barriers, with an agreement of better than 0.05 eV in every case. It thus appears that the activation barriers are largely insensitive to local components of the exchange-correlation functional, as well as to the use of range-correction in the representation of exchange. We conclude that the large difference between the PBE results and the HSE results is primarily a consequence of the inclusion of exact exchange.

Fig. 3(a) shows an additional path, denoted Path 2b, which has reactant and product states that are symmetrically identical to those of Path 2; however, because of the asymmetry of the Mo-O$_{(2)}$ bonds, the activation barrier of Path 2b is different from that of Path 2. Fig. 3(b) shows the results of NEB calculations of Path 2b. Interestingly, the PBE and HSE functionals qualitatively disagree regarding the relative activation barriers of Paths 2 and 2b. Using the PBE functional, the activation barrier of Path 2b is found to be 0.13 eV higher than that of Path 2, while the HSE functional indicates that the activation barrier of Path 2b is 0.12 eV lower than that of Path 2.

Fig. 4 demonstrates the importance of relaxing the nuclear geometry using a hybrid functional, rather than performing single-point hybrid calculations that use geometries obtained with a
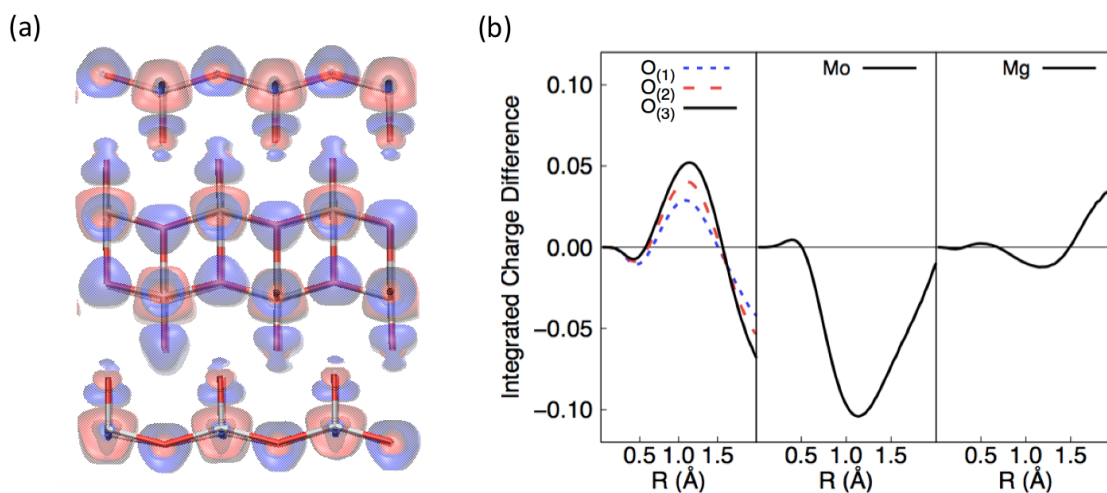
Fig. 1 (a) Comparison of the PBE and HSE//PBE electronic densities. The difference between the PBE and HSE//PBE densities is shown by an isosurface of +/- 0.002. The isosurface is colored blue where the HSE//PBE density is higher and red where the HSE//PBE density is lower. Molybdenum atoms are colored white, while oxygen atoms are colored red. (b) Electronic density difference between PBE and HSE//PBE calculations, integrated within a sphere of radius R around nuclei of the indicated types, with positive values indicating a higher HSE density. Results are provided for each of the three symmetrically distinct oxygen nuclei ($O_{(1)}$, $O_{(2)}$, and $O_{(3)}$), a molybdenum nucleus (Mo), and a magnesium nucleus (Mg). The magnesium results are obtained from a configuration corresponding to the reactant state of Path 1 (see Fig. 2(a)); all other results are obtained using a PBE-optimized supercell that does not contain any Mg nuclei.

semi-local functional. The black solid curves in Fig. 4 show the result of performing single-point HSE calculations on each of the images obtained from a PBE NEB calculation, which we denote as HSE//PBE NEB calculations. Compared to the fully-relaxed HSE NEB calculations (shown by the blue dotted curves), the HSE//PBE NEB results exhibit a significantly lower energy for the product state of Paths 1 and 2 and for the transition state of Paths 2 and 3. These results indicate that the popular approach of performing single-point hybrid DFT calculations using geometries obtained with non-hybrid functionals is not suitable for this system.

In order to more precisely identify which nuclei must be relaxed for an accurate treatment of this system, additional single-point HSE calculations are performed using nuclear configurations obtained by combining the lattice geometry from the PBE NEB calculations with the Mg^{2+} ion position from the HSE NEB calculations. As shown by the brown dashed curves in Fig. 4, the results of these calculations are consistently slightly worse than the results of the HSE//PBE calculations. Conversely, another set of HSE calculations are performed using configurations obtained by combining the lattice geometry from the HSE NEB calculations with the Mg^{2+} ion position from the PBE NEB calculations. As shown by the purple dashed-dotted curves in Fig. 4, the results of these calculations more closely agree with the fully-relaxed HSE NEB calculations. From this observation, we conclude that HSE-level relaxation of the α-MoO$_3$ lattice is essential for an accurate understanding of the energetics of Mg-ion diffusion in this material.

We now examine the extent to which the large differences between the PBE and HSE energies in Fig. 2(b) and Fig. 3(b) are sensitive to the choice of pseudopotential. Fig. 5(a) presents the results of PBE (black solid curve) and HSE (blue

dotted curve) NEB calculations that are identical to those of Fig. 2(b), except that instead of using Schlipf-Gygi pseudopotentials we use norm-conserving Martins-Troullier type pseudopotentials from the Abinit pseudopotential database[81], generated using the fhi98PP code[82]. Consistent with the results in Fig. 2(b), the results in Fig. 5(a) show that relative to PBE, the HSE functional yields a lower activation barrier for Path 1 and a higher activation barrier for Paths 2 and 3. Additionally, the HSE forward reaction energy of Paths 1 and 2 is approximately 0.2 eV lower than the corresponding PBE reaction energy, which is a somewhat larger difference than was observed when using the Schlipf-Gygi pseudopotentials. Overall, we find that the effects of introducing hybrid exchange are robust with respect to the choice of pseudopotential. Further work may investigate the use of pseudopotentials developed specifically for hybrid functional calculations[83].

3.3 Comparison of GGA+U with hybrid DFT

The dashed orange and dashed-dotted green curves in Fig. 5(a) demonstrate that the inclusion of Hubbard U terms does not provide a straightforward approach to improving the accuracy of semi-local functionals for this system. These curves show the results of PBE NEB calculations that employ a Hubbard U of 4.0 eV that is either applied to only the molybdenum nuclei (dashed red curves) or to both the molybdenum and oxygen nuclei (dotted blue curves). Previous work has identified a molybdenum Hubbard U of approximately 4.0 eV as being optimal for reproducing the Mg intercalation voltage in α-MoO$_3$ and for reproducing the reaction enthalpies of various Mo compounds[21,22]. Fig. 5(a) shows that when the Hubbard U is applied only to the molybdenum nuclei, the results are largely unaffected, except that the energies of all configurations along Path 3 are somewhat increased relative to the other configurations. Application of a Hubbard U

(a)

(b)
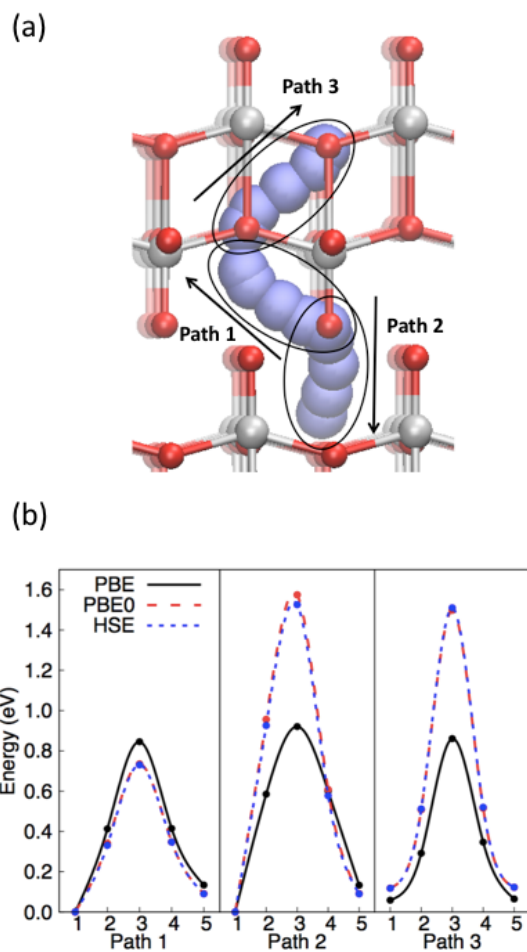
Fig. 2 (a) Three possible paths for Mg diffusion in the α-MoO$_3$ lattice. Molybdenum atoms are colored white, while oxygen atoms are colored red. The Mg-ion diffusion pathways are indicated by the blue spheres. The arrows next to each diffusion pathway indicate the direction that this work classifies as the forward diffusion process. (b) Energy profiles of each different path, obtained from NEB calculations using the PBE, PBE0, and HSE functionals.

(a)

(b)

Fig. 3 (a) An additional path, not shown in Fig. 2, that has starting and ending points that are symmetrically identical to those of Path 2, but having a different activation barrier. The structure of the α-MoO$_3$ lattice depicted in the image corresponds to the reactant state of Paths 2 and 2b. (b) Comparison of the energy profile of Path 2 (solid black curve) with Path 2b (red dashed curve) using both the PBE and HSE functionals.

to both the molybdenum and oxygen nuclei produces more pronounced effects, but does not systematically improve the agreement with the HSE results; in particular, the reaction energies of Paths 1 and 2, as well as the forward activation barrier of Path 1 are in poorer agreement with the corresponding HSE values.

Because of ambiguities in the proper method for selecting the value of the Hubbard U[24], we now examine the effects of applying different values of the Hubbard U to the oxygen nuclei. Figure 5(b) shows the difference between the PBE+U and HSE electronic densities of an α-MoO$_3$ supercell, as a function of the value of the Hubbard U that is applied to the oxygen nuclei, U_O. Specifically, we compute

$$\langle\, |\rho_{PBE+U} - \rho_{HSE}|\, \rangle = \frac{1}{N}\int_{cell} [|\rho_{PBE+U}(\mathbf{r}) - \rho_{HSE}(\mathbf{r})|]\, d\mathbf{r} \quad (4)$$

where ρ is the electronic density, N is the number of electrons, and the integration is performed over the entire supercell. Both ρ_{PBE+U} and ρ_{HSE} are obtained using nuclear coordinates that are

relaxed at the PBE level of theory. The results in Fig. 5(b) show that the difference between the PBE+U and HSE electronic densities is minimized at approximately $U_O = 4.0$ eV, with nearly a twofold improvement compared to $U_O = 0.0$ eV. Values of $U_O = 8.0$ eV or greater are found to produce results of decreasing agreement with HSE.

We note that by itself, Fig. 5(b) might be interpreted as suggesting that the use of $U_O = 4.0$ eV could improve the results of PBE calculations involving this system. This conclusion would unfortunately be inaccurate in view of the PBE+U results in Fig. 5(a). Furthermore, Fig. 5(c) shows that the errors in the PBE+U reaction energy of Path 1 monotonically increase with the addition of a U_O in the range of 0.0-16.0 eV. It is thus clear that values of U_O that yield improved representations of the electronic density distribution do not necessarily lead to improvements in the nuclear potential energy surface of Mg diffusion in α-MoO$_3$. From
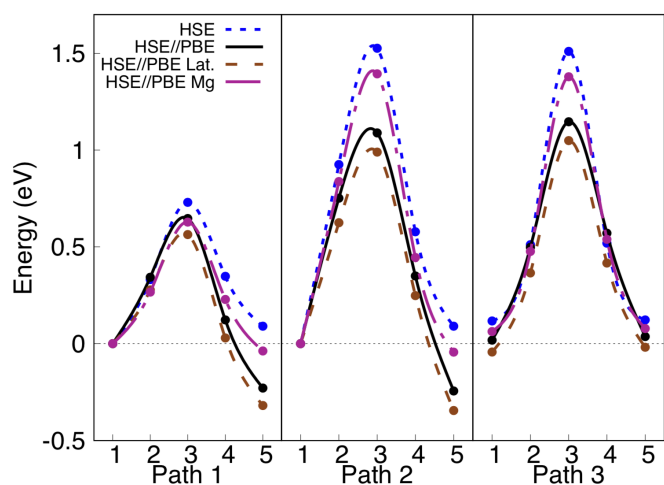
Fig. 4 The blue dotted curves provide the HSE NEB energies (identical to the blue dotted curves in Fig. 2(b)), while the black solid curves provide the single-point HSE energies of the PBE NEB images. The brown dashed curves provide the single-point HSE energies of configurations obtained by combining the lattice geometry from the PBE NEB calculations with the Mg^{2+} ion position from the HSE NEB calculations. The purple dashed-dotted curves provide the single-point HSE energies of configurations obtained by combining the lattice geometry from the HSE NEB calculations with the Mg^{2+} ion position from the PBE NEB calculations. Each curve is shifted to zero at the first image of Path 1.

this observation, we conclude that the PBE+U approach is not capable of reasonably approximating the results of hybrid functionals for this system, even if special effort is made to identify the optimal Hubbard U parameters.

4 Conclusions

We have evaluated the energetics of Mg ion diffusion in α-MoO$_3$ using computationally demanding hybrid functionals. Of the three diffusive paths considered in this paper, hybrid functionals predict that two are largely thermodynamically inaccessible, suggesting that diffusion of Mg ions through the bulk material should be negligible over the course of a typical charge/discharge cycle in an Mg-ion battery. This contrasts with the results of the semi-local PBE functional, which yields significantly smaller energy barriers for bulk diffusion. Moreover, inclusion of a Hubbard U parameter in the semi-local calculations does not improve the agreement between the semi-local and hybrid results.

Our observations are consistent with the results of numerous prior studies on the importance of exact exchange in the treatment of localized d electrons in transition metal oxides.[22–27] These studies have compellingly established the limitations of GGA functionals in accurately representing equilibrium properties, such as bond lengths, lattice constants, and band gaps. Less thoroughly studied has been the effect of hybrid DFT on simulated reaction paths and activation barriers. By performing highly computationally demanding NEB calculations in which the nuclear coordinates are relaxed using hybrid DFT, we have demonstrated the inadequacy of the GGA and GGA+U approaches for investigation of Mg ion diffusion in α-MoO$_3$. In particular, the introduction of a single Hubbard U for the oxygen nuclei is not in-

dependently sufficient to improve the computed potential energy surface. It is possible that more complex approaches, such as the use of different values of the Hubbard U for each oxygen type or the DFT+U+J method[84] are capable of greater accuracy, but at the expense of a larger number of tunable parameters. Moreover, we find that attempts to avoid the computational cost of fully-relaxed HSE calculations by instead performing HSE//PBE calculations lead to results that are largely inferior to those of PBE calculations. Accurate simulation of Mg ion diffusion in α-MoO$_3$ thus necessitates the use of hybrid functionals both for relaxation of the nuclear coordinates and for evaluation of the electronic density distribution.

Similar studies on other metal oxides and related systems will be necessary to evaluate the full scope of these conclusions, although the fundamental nature of the approximations inherent to GGA and GGA+U suggests the likelihood that this scope is broad. This work may be interpreted as a cautionary example of the crucial necessity for validating the applicability of semi-local functionals prior to their utilization. Further progress in the simulation of ion diffusion in transition-metal oxides will require careful attention to the treatment of exchange, with a combination of methodological improvements and algorithmic advances being essential for enabling more wide-spread application of hybrid functionals.

Acknowledgments

References

1 D. Aurbach, Z. Lu, A. Schechter, Y. Gofer, H. Gizbar, R. Turgeman, Y. Cohen, M. Moshkovich and E. Levi, *Nature*, 2000, **407**, 724.

2 H. D. Yoo, I. Shterenberg, Y. Gofer, G. Gershinsky, N. Pour and D. Aurbach, *Energy & Environmental Science*, 2013, **6**, 2265–2279.

3 Y. Orikasa, T. Masese, Y. Koyama, T. Mori, M. Hattori, K. Yamamoto, T. Okado, Z.-D. Huang, T. Minato, C. Tassel *et al.*, *Scientific reports*, 2014, **4**, year.

4 J. O. Besenhard and M. Winter, *ChemPhysChem*, 2002, **3**, 155–159.
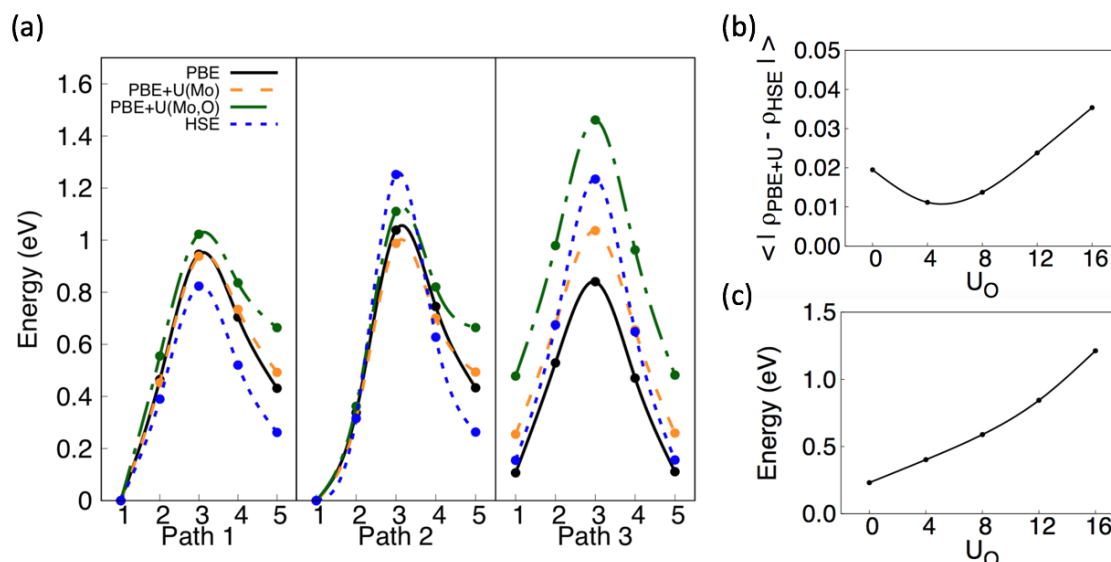
Fig. 5 Results obtained using pseudopotentials from the Abinit database. (a) The black solid curves show the results of PBE NEB calculations, the orange dashed curves show the results of PBE NEB calculations with a Hubbard U of 4.0 eV applied to the molybdenum nuclei, the green dashed-dotted curves show the results of PBE NEB calculations with a Hubbard U of 4.0 eV applied to both the molybdenum and oxygen nuclei, and the blue dotted curves show the results of HSE NEB calculations. The nuclear coordinates in each NEB calculation are obtained using the corresponding level of theory, and each curve is shifted to zero at the first image of Path 1 (b) Integrated error in the α-MoO$_3$ cell electronic density, $\langle |\rho_{PBE+U} - \rho_{HSE}| \rangle$ (see Eq. 4), as a function of the oxygen Hubbard U, U_O. In each case, a Hubbard U of 4.0 eV is applied to the molybdenum nuclei. (c) Error in the PBE+U forward reaction energy of Path 1, relative to the HSE reaction energy, as a function of U_O. In each case, a Hubbard U of 4.0 eV is applied to the molybdenum nuclei, and the nuclear coordinates are relaxed at the PBE+U level of theory.

5 M. M. Huie, D. C. Bock, E. S. Takeuchi, A. C. Marschilok and K. J. Takeuchi, *Coordination Chemistry Reviews*, 2015, **287**, 15–27.

6 E. Levi, Y. Gofer and D. Aurbach, *Chemistry of Materials*, 2009, **22**, 860–868.

7 H. Yuan, L. Jiao, J. Cao, X. Liu, M. Zhao and Y. Wang, *Journal of Materials Science and Technology*, 2004, **20**, 41–45.

8 Y. Liang, R. Feng, S. Yang, H. Ma, J. Liang and J. Chen, *Advanced Materials*, 2011, **23**, 640–643.

9 Z. Wang, Q. Su and H. Deng, *Physical Chemistry Chemical Physics*, 2013, **15**, 8705–8709.

10 S. Yang, D. Li, T. Zhang, Z. Tao and J. Chen, *The Journal of Physical Chemistry C*, 2011, **116**, 1307–1312.

11 X. Sun, V. Duffort, B. L. Mehdi, N. D. Browning and L. F. Nazar, *Chem. Mater*, 2016, **28**, 534–542.

12 S. Tepavcevic, Y. Liu, D. Zhou, B. Lai, J. Maser, X. Zuo, H. Chan, P. Král, C. S. Johnson, V. Stamenkovic et al., *ACS nano*, 2015, **9**, 8194–8205.

13 G. Gershinsky, H. D. Yoo, Y. Gofer and D. Aurbach, *Langmuir*, 2013, **29**, 10964–10972.

14 P. Novák, R. Imhof and O. Haas, *Electrochimica Acta*, 1999, **45**, 351–367.

15 M. Spahr, P. Novak, O. Haas and R. Nesper, *Journal of power sources*, 1995, **54**, 346–351.

16 J. W. Bullard III and R. L. Smith, *Solid State Ionics*, 2003, **160**, 335–349.

17 J. Muldoon, C. B. Bucur and T. Gregory, *Chemical reviews*, 2014, **114**, 11683–11720.

18 X. Hu, W. Zhang, X. Liu, Y. Mei and Y. Huang, *Chemical Society Reviews*, 2015, **44**, 2376–2404.

19 G. Pandey, R. Agrawal and S. Hashmi, *Journal of Solid State Electrochemistry*, 2011, **15**, 2253–2264.

20 P. Canepa, G. Sai Gautam, D. C. Hannah, R. Malik, M. Liu, K. G. Gallagher, K. A. Persson and G. Ceder, *Chemical reviews*, 2017, **117**, 4287–4341.

21 L. F. Wan, J. T. Incorvati, K. R. Poeppelmeier and D. Prendergast, *Chemistry of Materials*, 2016, **28**, 6900–6908.

22 G. Hautier, S. P. Ong, A. Jain, C. J. Moore and G. Ceder, *Physical Review B*, 2012, **85**, 155208.

23 L. Wang, T. Maxisch and G. Ceder, *Physical Review B*, 2006, **73**, 195107.

24 S. Lutfalla, V. Shapovalov and A. T. Bell, *Journal of chemical theory and computation*, 2011, **7**, 2218–2223.

25 W. Yang and P. W. Ayers, *Computational Medicinal Chemistry for Drug Discovery*, CRC Press, 2003, pp. 103–132.

26 A. J. Cohen, P. Mori-Sánchez and W. Yang, *Science*, 2008, **321**, 792–794.

27 B. Himmetoglu, A. Floris, S. De Gironcoli and M. Cococcioni, *International Journal of Quantum Chemistry*, 2014, **114**, 14–49.

28 B. Liu, T. Luo, G. Mu, X. Wang, D. Chen and G. Shen, *ACS nano*, 2013, **7**, 8051–8058.

29 O. I. Malyi, T. L. Tan and S. Manzhos, *Journal of Power Sources*, 2013, **233**, 341–345.

30 O. Malyi, V. V. Kulish, T. L. Tan and S. Manzhos, *Nano Energy*, 2013, **2**, 1149–1157.

31 F. Legrain, O. I. Malyi and S. Manzhos, *Solid State Ionics*, 2013, **253**, 157–163.

32 J. Shuai, H. D. Yoo, Y. Liang, Y. Li, Y. Yao and L. C. Grabow, *Transition*, 2016, **12**, 14.

33 B. Zhou, H. Shi, R. Cao, X. Zhang and Z. Jiang, *Physical Chemistry Chemical Physics*, 2014, **16**, 18578–18585.

34 D. O. Scanlon, A. Walsh, B. J. Morgan and G. W. Watson, *The Journal of Physical Chemistry C*, 2008, **112**, 9903–9911.

35 A. O. Pereira and C. R. Miranda, *The Journal of Physical Chemistry C*, 2015, **119**, 4302–4311.

36 P. Canepa, J. A. Dawson, G. Sai Gautam, J. M. Statham, S. C. Parker and M. S. Islam, *Chemistry of Materials*, 2018, **30**, 3019–3027.

37 Y. Deng, C. Eames, L. H. Nguyen, O. Pecher, K. J. Griffith, M. Courty, B. Fleutot, J.-N. Chotard, C. P. Grey, M. S. Islam *et al.*, *Chemistry of Materials*, 2018, **30**, 2618–2630.

38 R. Brenes, D. Guo, A. Osherov, N. K. Noel, C. Eames, E. M. Hutter, S. K. Pathak, F. Niroui, R. H. Friend, M. S. Islam *et al.*, *Joule*, 2017, **1**, 155–167.

39 J. D. Baran, C. Eames, K. Takahashi, M. Molinari, M. S. Islam and S. C. Parker, *Chemistry of Materials*, 2017, **29**, 7364–7370.

40 J. A. Dawson, A. J. Naylor, C. Eames, M. Roberts, W. Zhang, H. J. Snaith, P. G. Bruce and M. S. Islam, *ACS Energy Letters*, 2017, **2**, 1818–1824.

41 N. Aristidou, C. Eames, I. Sanchez-Molina, X. Bu, J. Kosco, M. S. Islam and S. A. Haque, *Nature Communications*, 2017, **8**, 15218.

42 J. Heath, H. Chen and M. S. Islam, *Journal of Materials Chemistry A*, 2017, **5**, 13161–13167.

43 T. Kaewmaraya, M. Ramzan, J. Osorio-Guillen and R. Ahuja, *Solid State Ionics*, 2014, **261**, 17–20.

44 K. M. Bui, V. A. Dinh, S. Okada and T. Ohno, *Physical Chemistry Chemical Physics*, 2015, **17**, 30433–30439.

45 Y. Yuan, C. Zhan, K. He, H. Chen, W. Yao, S. Sharifi-Asl, B. Song, Z. Yang, A. Nie, X. Luo *et al.*, *Nature communications*, 2016, **7**, 13374.

46 H. Chen and M. S. Islam, *Chemistry of Materials*, 2016, **28**, 6656–6663.

47 F. Oba, A. Togo, I. Tanaka, J. Paier and G. Kresse, *Physical Review B*, 2008, **77**, 245202.

48 J.-C. Wu, J. Zheng, P. Wu and R. Xu, *The Journal of Physical Chemistry C*, 2011, **115**, 5675–5682.

49 M. Harb, *The Journal of Physical Chemistry C*, 2013, **117**, 12942–12948.

50 J. Liu, *The Journal of Physical Chemistry C*, 2015, **119**, 28417–28423.

51 B. Modak, K. Srinivasu and S. K. Ghosh, *Physical Chemistry Chemical Physics*, 2014, **16**, 24527–24535.

52 J. Liu and E. Hua, *The Journal of Physical Chemistry C*, 2017, **121**, 25827–25835.

53 H. Fang and P. Jena, *Journal of Materials Chemistry A*, 2016, **4**, 4728–4737.

54 J. Zhang, S. Wageh, A. Al-Ghamdi and J. Yu, *Applied Catalysis B: Environmental*, 2016, **192**, 101–107.

55 J. T. Dufton, A. Walsh, P. M. Panchmatia, L. M. Peter, D. Colombara and M. S. Islam, *Physical Chemistry Chemical Physics*, 2012, **14**, 7229–7233.

56 J. Paier, R. Asahi, A. Nagoya and G. Kresse, *Physical Review B*, 2009, **79**, 115126.

57 F. Wang, C. Di Valentin and G. Pacchioni, *The Journal of Physical Chemistry C*, 2011, **115**, 8345–8353.

58 N. Nilius, H. Fedderwitz, B. Groß, C. Noguera and J. Goniakowski, *Physical Chemistry Chemical Physics*, 2016, **18**, 6729–6733.

59 T. A. Barnes, T. Kurth, P. Carrier, N. Wichmann, D. Prendergast, P. R. Kent and J. Deslippe, *Computer Physics Communications*, 2017, **214**, 52–58.

60 L. Lin, *Journal of chemical theory and computation*, 2016, **12**, 2242–2249.

61 P. Giannozzi, S. Baroni, N. Bonini, M. Calandra, R. Car, C. Cavazzoni, D. Ceresoli, G. L. Chiarotti, M. Cococcioni, I. Dabo *et al.*, *Journal of physics: Condensed matter*, 2009, **21**, 395502.

62 F. Gygi, *Physical review letters*, 2009, **102**, 166406.

63 F. Neese, F. Wennmohs, A. Hansen and U. Becker, *Chemical Physics*, 2009, **356**, 98–109.

64 R. A. DiStasio Jr, B. Santra, Z. Li, X. Wu and R. Car, *The Journal of chemical physics*, 2014, **141**, 084502.

65 P. Giannozzi, O. Andreussi, T. Brumme, O. Bunau, M. B. Nardelli, M. Calandra, R. Car, C. Cavazzoni, D. Ceresoli, M. Cococcioni *et al.*, *Journal of Physics: Condensed Matter*, 2017, **29**, 465901.

66 J. P. Perdew and A. Zunger, *Physical Review B*, 1981, **23**, 5048.

67 C. Toher and S. Sanvito, *Physical review letters*, 2007, **99**, 056801.

68 M. Ribeiro Jr, L. R. Fonseca and L. G. Ferreira, *Physical Review B*, 2009, **79**, 241312.

69 L. G. Ferreira, M. Marques and L. K. Teles, *Aip Advances*, 2011, **1**, 032119.

70 S. Dudarev, G. Botton, S. Savrasov, C. Humphreys and A. Sutton, *Physical Review B*, 1998, **57**, 1505.

71 http://www.nersc.gov.

72 J. P. Perdew, K. Burke and M. Ernzerhof, *Physical review letters*, 1996, **77**, 3865.

73 J. Heyd, G. E. Scuseria and M. Ernzerhof, *The Journal of Chemical Physics*, 2003, **118**, 8207–8215.

74 D. Hamann, *Physical Review B*, 2013, **88**, 085117.

75 M. Schlipf and F. Gygi, *Computer Physics Communications*, 2015, **196**, 36–44.

76 P. Mori-Sánchez, A. J. Cohen and W. Yang, *Many-electron self-interaction error in approximate density functionals*, 2006.

77 J. Autschbach and M. Srebro, *Accounts of chemical research*, 2014, **47**, 2592–2602.

78 J. Paier, *Catalysis Letters*, 2016, **146**, 861–885.

79 J. P. Perdew, M. Ernzerhof and K. Burke, *The Journal of Chemical Physics*, 1996, **105**, 9982–9985.

Physical Chemistry Chemical Physics

80 C. Adamo and V. Barone, *The Journal of chemical physics*, 1999, **110**, 6158–6170.

81 X. Gonze, J.-M. Beuken, R. Caracas, F. Detraux, M. Fuchs, G.-M. Rignanese, L. Sindic, M. Verstraete, G. Zerah, F. Jollet *et al.*, *Computational Materials Science*, 2002, **25**, 478–492.

82 M. Fuchs and M. Scheffler, *Journal reference: Comput. Phys. Commun*, 1999, **119**, 67.

83 J. Yang, L. Z. Tan and A. M. Rappe, *Physical Review B*, 2018, **97**, 085130.

84 B. Himmetoglu, R. M. Wentzcovitch and M. Cococcioni, *Physical Review B*, 2011, **84**, 115108.